INTERNATIONAL JOURNAL FOR NUMERICAL METHODS IN FLUIDS
Int. J. Numer. Meth. Fluids 2001; **36**: 391–416 (DOI: 10.1002/fld.134)

A new multi-domain/multi-resolution method for large-eddy simulation

Patrick Quéméré, Pierre Sagaut*,[1] and Vincent Couailler

ONERA/DSNA, 29 av. de la Division Leclerc, 92322 Châtillon Cedex, France

SUMMARY

A new multi-domain/multi-resolution method is presented in the framework of the large-eddy simulation (LES). The proposed treatment at the interfaces is conceived to deal with the problem of discontinuities on the characteristic length scales met in the case of two domains having different resolutions. It gives rise to an original approach taking into account not only the discontinuous aspect on the flow fields values but also, consequently, the non-conservative aspect of transfer of fluxes through the interfaces. This new treatment at the interfaces has been assessed successfully in the case of a subsonic compressible channel flow. Copyright © 2001 John Wiley & Sons, Ltd.

KEY WORDS: channel flow; large-eddy simulation; multi-domain; multi-resolution

1. INTRODUCTION

With recent advances in computer capacity, the interest in large-eddy simulation (LES) has increased over the last few years. The reason for this interest is that LES offers a nice compromise between CPU costs and accuracy of the calculated results, when compared with the Reynolds-averaged Navier-Stokes (RANS) approach and to direct numerical simulation (DNS), which is very accurate but requires large amounts of memory. The former approach, used in industrial codes for complex configurations, predicts statistical moments of the solution and can be applied to very complex geometries. Presently, the latter is only used in simple configurations at low Reynolds number because of the very high cost of calculations resolving all the turbulence length scales. LES appears like an appropriate tool to predict more accurately the dynamics of unsteady flows.

It is based on the computation of large scales by solving filtered Navier–Stokes equations and modelling the effects of the smaller scales, referred to as the sub-grid scale (SGS) terms. Classical models for LES are built from the local isotropy hypothesis. It implies that the

* Correspondence to: ONERA, DSNA/ETRI, 29 av. de la Division Leclerc, 92322 Châtillon Cedex, France. Tel.: + 33 1 46734271; fax: + 33 1 43734166.
[1] E-mail: sagaut@onera.fr

Received 20 December 1999
Revised 7 June 2000

characteristic cut-off length scale of the filter is sufficiently small to be located in the inertial range of turbulence. Because this characteristic length is linked with the spatial discretization (mesh size), and because very small coherent anisotropic structures exist, in particular near the walls, the computational grids used in the LES computations have to be locally refined in such a way that these structures are directly captured by the simulation.

For that purpose, two approaches are possible: one using unstructured meshes and a second one using structured meshes.

The first one makes it possible to refine the mesh in the near wall regions while, as expected, reducing gradually the number of grid points far away from the solid boundaries, where the dynamics are much simpler to capture. Conceptually, this approach is very attractive and allows a continuous treatment of all quantities. It raises the problem, however, of data structures for recognition of the adjacent cells.

The other approach is more classical. With structured meshes, if the refinement can be done easily in the wall-normal direction, the streamwise and spanwise grid resolutions are generally maintained throughout the whole computational domain. A possibility to reduce this excessive resolution is to increase the mesh size by using several domains. Using this method, sudden changes in mesh size and thus in characteristic lengths exist at the interfaces.

Among the authors who have developed this type of multi-domain approach, most of them developed a continuous treatment for the variables at the interface of each domain.

For the plane channel application case, Simons *et al.* [1], from works of Rai [2,3] and Kallinderis [4], carried out different interface procedures in LES in order to maintain continuous behaviour at the interface. All these works are based on the principle of flux conservation. The only cases considered have been for a unique value of the *mesh ratio* at the interface (ref. [2] in the cited study). Kravchenko *et al.* [5], for zonal embedded grids, proposed to use a Galerkin method with B-spline basis function to perform LES of the channel flow. This method was recently extended to curvilinear grids [6].

In a radically different way, this paper proposes a new concept based on a non-overlapping multi-domain approach involving a discontinuity in the resolved variables in order to take into account the different characteristic lengths observed along the interfaces. A coupling method based on the reconstruction of ghost-cell values, well suited for cell-centred finite volume techniques, is developed and assessed.

This paper is thus organized as follows: after having established the fundamental equations and the modeling for LES approach in Sections 2 and 3, this paper in Section 4 justifies using a non-conservative transfer of fluxes and a discontinuous flow field at the interface. A multi-domain/multi-resolution algorithm is thus set out in order to take into account this discontinuity. Section 5 is devoted to a brief description of the numerical method. Section 6, after having defined the physical problem and parameters, presents the results obtained on a subsonic plane channel flow configuration at Mach number $M_0 = 0.5$ with the multi-domain/multi-resolution technique proposed here.

First, the results obtained in a mono-domain case are compared and discussed with respect to Lenormand *et al.*'s results [7,8] in order to validate the basic method. Then, an *a priori* assessment of the SGS viscosity reconstruction procedure is carried out and a presentation about different results obtained by using the multi-domain/multi-resolution algorithm applied for two Reynolds numbers and three different values of the mesh ratio between the domains

at the interface, are presented at the end of Section 6. Finally, a conclusion is drawn in Section 7.

2. GOVERNING EQUATIONS

LES is based on the spatially filtered equations of motion. The filtering operation is defined from a mathematical point of view for the dummy variable ϕ as a convolution product

$$\bar{\phi} = \int_{\Omega} G(x-\xi;\ \Delta)\phi(\xi)\,\mathrm{d}\xi \tag{1}$$

where G is the kernel filter function and Δ is the cut-off length scale associated with the filter. Any flow variable ϕ in the fluid domain Ω can be decomposed into a large scale part $\bar{\phi}$ and a small scale part ϕ' respectively as follows:

$$\phi = \bar{\phi} + \phi' \tag{2}$$

The LES governing equations are obtained by implicitly applying this type of filtering operator to Navier–Stokes equations. This operation introduces sub-grid terms. When filtered equations are rewritten in an analogous form to the non-filtered equations, it is convenient to employ the related density weighted variables given by Favre [9] as

$$\tilde{\phi} = \frac{\overline{\rho\phi}}{\bar{\rho}} \tag{3}$$

Using this mass-weighted filter, the variable ϕ is further decomposed as

$$\phi = \tilde{\phi} + \phi''$$

The resulting filtered non-dimensional compressible Navier–Stokes equations for conservation of mass, momentum and total energy are written as

$$\partial_t\bar{\rho} + \partial_j(\bar{\rho}\tilde{u}_j) = 0$$

$$\partial_t(\bar{\rho}\tilde{u}_i) + \partial_j(\bar{\rho}\tilde{u}_i\tilde{u}_j + \bar{p} - \hat{\sigma}_{ij}) = -A_1 + A_2$$

$$\partial_t\hat{E} + \partial_j((\hat{E} + \bar{p})\tilde{u}_j - \hat{\sigma}_{ij}\tilde{u}_i + \hat{q}_j) = -B_1 - B_2 - B_3 + B_4 + B_5 + B_6 - B_7 \tag{4}$$

where the A_1, A_2, $B_1, \ldots, B_7$ terms are the sub-grid terms coming from Vreman's decomposition [10,11] and used by Lenormand *et al.* [7,8]. Symbols ∂_t and ∂_j denote the time derivative and the divergence operator respectively. The summation convention for repeated indices is used.

The modified filtered viscous stress tensor $\widehat{\sigma_{ij}} = \sigma_{ij}(\tilde{T}; \tilde{u})$, heat flux $\widehat{q_j} = q_j(\tilde{T})$ and energy $\hat{E} = E(\bar{p}; \bar{\rho}; \tilde{u})$ are defined on the basis of the non-filtered non-dimensional quantities

$$\sigma_{ij} = \sigma_{ij}(T; u) = (\mu(T)/Re)\cdot(\partial_j u_i + \partial_i u_j - 2\delta_{ij}\partial_k u_k/3)$$

$$q_j = q_j(T) = -\mu(T)/((\gamma - 1)RePrM_0^2)\,\partial_j T$$

$$E = E(p; \rho; u) = p/(\gamma - 1) + \rho u_j u_j/2 \tag{5}$$

The Prandtl number Pr and the ratio γ of the specific heats C_p and C_v are taken equal to $Pr = 0.7$ and $\gamma = 1.4$. The dynamic viscosity $\mu(T)$ is expressed by Sutherland's Law for air $\mu(T) = T^{3/2}(1 + C)/(T + C)$, with $C = 0.4$. All these equations have been made dimensionless by introducing a reference length L_R, velocity u_R, density ρ_R and temperature T_R. The values of the Reynolds number $Re = \rho_R u_R L_R/\mu(T_R)$ and the Mach number M_0 will be detailed in Section 6.

The set of filtered Navier–Stokes equations is finally completed by the filtered state law

$$\bar{p} = \bar{\rho}\tilde{T}/(\gamma M_0^2) \tag{6}$$

3. SUB-GRID MODELLING

Several assumptions allow us to simplify the expressions given above in Equation (4) by neglecting some terms in the filtered equations for the present computation. Following Vreman's conclusions [10], the A_2, B_7 and B_6 terms can be neglected. Also according to Reference [10], the B_5 and B_4 terms are small with respect to B_1, B_2 and B_3 in the energy equation and will be neglected too. It is important noting that these assumptions have been shown to remain valid in compressible channel flow by *a priori* tests [8].

Finally, sub-grid models for A_1 in the momentum equation and B_1, B_2 and B_3 in the energy equation are necessary to close the problem. It is worth noting that similar hypotheses have been used by Vreman *et al.* [11] and Moin *et al.* [12]. Considering sub-grid viscosity type models relying on the Boussinesq hypothesis, we get

$$A_1 = \partial_j \tau_{ij}$$

$$B_3 = \partial_j \tau_{ij} \tilde{u}_i$$

$$B_1 + B_2 = -\partial_j\left(\frac{\bar{\rho}\tilde{\mu}_t}{(\gamma - 1)Pr_t M_0^2}\,\partial_j \tilde{T}\right) \tag{7}$$

where the deviatoric part τ_{ij}^D of the sub-grid scale stress tensor $\tau_{ij} = \bar{\rho}(\widetilde{u_i u_j} - \tilde{u}_i\tilde{u}_j)$ is modelled by

$$\tau_{ij}^{D} = \tau_{ij} - \frac{1}{3}\tau_{kk}\delta_{ij} = -\tilde{\mu}_t(\partial_j\tilde{u}_i + \partial_i\tilde{u}_j) = -2\tilde{\mu}_t\tilde{S_{ij}} \tag{8}$$

In this last equation, $S_{ij} = \frac{1}{2}(\partial_j\tilde{u}_i + \partial_i\tilde{u}_j)$ and $\tilde{\mu}_t$ denote the resolved strain tensor and the sub-grid viscosity respectively. The sub-grid Prandtl number Pr_t is set equal to 0.6.

The SGS viscosity $\tilde{\mu}_t$ is computed using the mixed scale model (MSM) proposed by Loc and Sagaut (see Reference [13] for a description). Its general form is given by using a non-linear combination of resolved vorticity $\tilde{\omega}$, the characteristic length scale $\tilde{\Delta}$ and the smallest resolved scale kinetic energy $\tilde{q_c^2} = \frac{1}{2}\widetilde{u_i'u_i'}$. In order to take into account structural information, a selective function f_{θ_0}, which depends on local angular fluctuation of the vorticity vector θ, is employed (see David [14] for the original form, and Lenormand *et al.* [7] and Sagaut *et al.* [13] for the modified form used in the present study). Finally, the SGS viscosity model is defined as

$$\tilde{\mu}_t = C\cdot f_{\theta_0}(\theta)\cdot\bar{\rho}\cdot|\tilde{\omega}|^{1/2}\cdot\tilde{\Delta}^{3/2}\cdot\tilde{q}_c^{1/2} \tag{9}$$

with $C = 0.06$. Using an evaluation procedure based on a test filter to estimate the smallest resolved scale kinetic energy (see References [7,13,15]), the sub-grid viscosity can be symbolically rewritten as a function of the characteristic length and the filtered field

$$\tilde{\mu}_t = \mu_t(\tilde{\mathbf{U}}; \tilde{\Delta}) \tag{10}$$

From this model the set of filtered equations of motion (4) can be rewritten in a simplified divergence form as

$$\partial_t\tilde{\mathbf{U}} + \nabla\cdot\mathbf{F}(\tilde{\mathbf{U}}) = 0 \tag{11}$$

where $\tilde{\mathbf{U}}$ is related to the vector of conservative filtered variables and $\mathbf{F}(\tilde{\mathbf{U}})$ includes the convective fluxes, the diffusive fluxes and SGS terms.

4. MULTI-DOMAIN/MULTI-RESOLUTION ALGORITHM

As stated in the introduction, it is very convenient to use several computational domains with different mesh sizes to optimize CPU costs. In this way we use fine meshes only where necessary to maintain reliable results.

In practice, the mesh size, the numerical scheme (and the sub-grid model [16]) define implicitly the LES filter during the numerical treatment of Navier–Stokes equations if the prefiltering technique is not applied. It is worth noting that most of the authors do not use that technique, making it impossible to characterize the effective filter associated to the computation. This problem is a general problem for the LES technique and all the related theoretical developments. The identification of the real LES filter remains an open problem which is out of scope of the present paper.

The multi-domain/multi-resolution will be first addressed in a theoretical way, practical implementation being discussed in a second step.

4.1. Theoretical setting of the problem

For the sake of simplicity, the problem of the discontinuity at the interface is illustrated considering a two-domain case.

The two domains are assumed to have different mesh sizes (i.e. different grid resolution) and thus two different cut-off length scales associated with two different filtering levels. These domains are noted Ω_c and Ω_f for the coarse mesh domain and for the fine mesh domain respectively. The discontinuity in the characteristic lengths along the domain interface Γ involves a discontinuity in the spectral representation of the flow field. To distinguish variables related to low-level resolution associated with the coarse mesh domain Ω_c from those referring to high-level resolution in the fine mesh domain Ω_f, a specific notation for each domain variable is introduced. The following notation is employed:

- Bar variables like $\bar{\omega}$, $\bar{\mu}_t$, $\bar{\Delta}$ refer to low-level resolution. $\bar{\omega}$ indicates an aerodynamic (conservative or primitive) variable, $\bar{\mu}_t$ the SGS viscosity and $\bar{\Delta}$ the characteristic length.
- Tilde variables like $\tilde{\omega}$, $\tilde{\mu}_t$, $\tilde{\Delta}$ are related to the same quantities but in the high-level resolution case. By definition, one sets $\tilde{\Delta} < \bar{\Delta}$.

For developed turbulence, in accordance with the notations previously given, the difference between the filters involves a discontinuous behaviour of the variables at the interface Γ

$$\tilde{\omega}|_\Gamma \neq \bar{\omega}|_\Gamma \tag{12}$$

This discontinuity on the filtered values affects naturally the fluctuating values. We decompose the aerodynamic field in each domain into its respective filtered and fluctuating parts

$$\omega = \tilde{\omega} + \omega'' \quad \text{on } \Omega_f$$

$$\omega = \bar{\omega} + \omega' \quad \text{on } \Omega_c$$

The discontinuity pointed out at the interface for filtered variables is automatically recovered by the fluctuating values, and thus, by the sub-grid viscosity, which accounts for the effects of the SGSs

$$\tilde{\omega}_\Gamma \neq \bar{\omega}_\Gamma \Rightarrow \omega''|_\Gamma \neq \omega'|_\Gamma \Rightarrow \tilde{\mu}_t|_\Gamma \neq \bar{\mu}_t|_\Gamma$$

Thus, in a general way fluxes are not conserved at the interface, neither in the weak nor in the strong sense

$$\int_\Gamma \mathbf{F}(\tilde{\mathbf{U}})\, \mathrm{d}\vec{S} \neq \int_\Gamma \mathbf{F}(\bar{\mathbf{U}})\, \mathrm{d}\vec{S} \quad \text{and} \quad \mathbf{F}(\tilde{\mathbf{U}})|_\Gamma \neq \mathbf{F}(\bar{\mathbf{U}})|_\Gamma \tag{13}$$

In order to transfer properly the information between the fine (high-frequency) domain Ω_f and the coarse (low-frequency) domain Ω_c without loosing accuracy in the high-frequency domain in the vicinity of the interface Γ, a coupling method has been defined. Such a coupling method

will depend implicitly on the features of the numerical method: finite volume/finite difference/finite elements, overlapping or non-overlapping sub-domains, flux- or pointwise value based approach, etc. We address here the case of a non-overlapping, pointwise value-based, multi-domain technique coupled to a cell-centred finite volume discretization. The coupling will be performed by reconstructing the *ad hoc* variables and the corresponding value of the sub-grid model in a row of ghost cells associated with each domain along the interface.

As a consequence, the coupling procedure acts directly on the computed variables, the modified fluxes being obtained directly from the reconstructed field at the interface. This is written as follows:

$$\Omega_f \to \Omega_c\text{: } \tilde{\omega}|_\Gamma = \mathscr{C}(\tilde{\omega}|_\Gamma) \quad \text{(fine to } \mathscr{C}\text{oarse)} \tag{14}$$

$$\Omega_c \to \Omega_f\text{: } \tilde{\omega}|_\Gamma = \mathscr{F}(\bar{\omega}|_\Gamma) \quad \text{(coarse to } \mathscr{F}\text{ine)} \tag{15}$$

where $\mathscr{C}$ and $\mathscr{F}$ are operators defined at the interface. As the proposed coupling method acts directly with the flow field and can be interpreted as a frequential restriction (for $\mathscr{C}$) and a frequential enrichment (for $\mathscr{F}$), we will in the future refer to the different procedures simply as: 'restriction' and 'enrichment'.

From a theoretical point of view, it is deduced from Equations (14) and (15) that

$$\mathscr{C} \circ \mathscr{F} = \mathscr{F} \circ \mathscr{C} = Id \tag{16}$$

where *Id* is the identity operator. Practical discrete implementation of these procedures is now described in the next two sections.

4.2. Restriction procedure

Considering relationship (14), the restriction procedure $\mathscr{C}$, which takes place in the 'coarse' ghost cells embedded in the fine domain Ω_f (see Figure 1), would have to be defined such that

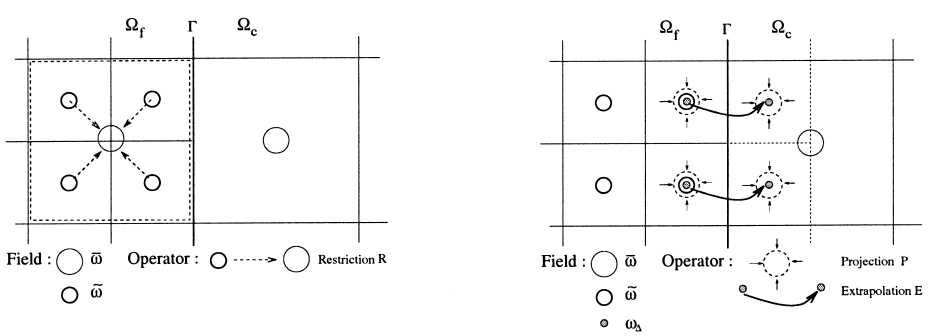

Figure 1. Schematic representation of restriction and enrichment procedure.

$$\mathscr{C} \circ \tilde{\cdot} \equiv \bar{\cdot} \tag{17}$$

It is worth noting that from a theoretical point of view, explicit knowledge of the LES filter associated with each domain is not required to build the restriction operator: one only needs relationship (17) to be satisfied. However, in practice, in order to define such a restriction operator, these two filters should be known. In order to be consistent with the finite volume approach, it is assumed that the filter associated to each computational is the box filter associated to the average over the control cell (possible contributions of the numerical error and sub-grid model are not taken into account).

Referred to as **R** or the restriction operator from now on, this filtering operator is defined in a continuous sense for a filtering length $\hat{\Delta}$ by the following convolution kernel:

$$G(x-\xi;\hat{\Delta}) = \begin{cases} \dfrac{1}{\hat{\Delta}} & \text{if } |x-\xi| \geq \dfrac{\hat{\Delta}}{2} \\ 0 & \text{else} \end{cases} \tag{18}$$

From a discrete point of view, this filtering is approximated to the second-order by a linear combination of n pointwise values contained in a box of size $\hat{\Delta}^3$

$$\hat{\omega} \equiv \mathbf{R}\tilde{\omega} = \frac{1}{n} \cdot \left(\sum_{p=1,n} \tilde{\omega}_p \right) \tag{19}$$

It is now assumed that the restriction operator $\mathscr{C}$ can be defined as a box filter with a characteristic length equal to $\bar{\Delta}$. It is worth noting here an important difference between continuous and discrete formulations of the box filter. Considering the continuous form of the filter will make some discrepancies appear, while this assumption is exact when the discrete box filters are retained. The associated discrete restriction operator is

$$\bar{\omega} \equiv \mathbf{R}\tilde{\omega} = \frac{1}{\sum_{p=1,n} \mathrm{Vol}_p} \cdot \left(\sum_{p=1,n} \tilde{\omega}_p \cdot \mathrm{Vol}_p \right) \tag{20}$$

with

$$\sum_{p=1,n} \mathrm{Vol}_p = \mathrm{Vol}_{\text{coarse cell}}$$

which equals the volume of the 'equivalent' coarse ghost cell, comprised of n fine cells. For a local mesh ratio r in the three space directions, this control volume includes r^3 fine cells.

The relative simplicity of this restriction procedure **R** allows us to define several rows of coarse ghost cells in the direction normal to the interface Γ and thus, to define properly the sub-grid viscosity $\bar{\mu}_{t\Omega_f}$ associated with characteristic length $\bar{\Delta}$ by using the same model as those used for current points on the coarse mesh. Finally, the reconstructed sub-grid viscosity associated with the low resolution level on Ω_f depends only on $\tilde{\mathbf{U}}$ and $\bar{\Delta}$

$$\bar{\mu}_{t\Omega_c} = \bar{\mu}_{t\Omega_f}(\tilde{\mathbf{U}}; \bar{\Delta}) \tag{21}$$

4.3. Enrichment procedure

The enrichment procedure characterized previously by the operator $\mathscr{F}$ is much more difficult to conceive than the former procedure. This procedure can be interpreted as a defiltering or deconvolution procedure, with some high frequencies being regenerated. Several attempts to build such a procedure have been proposed by previous authors, relying on the construction of discrete inverse operator for the box filter [17,18], sometimes coupled to a kinematic reconstruction step for the high frequencies [19,20]. We propose here a different approach, which accounts explicitly for the information contained in the fine-resolution sub-domain.

The basic idea proposed here is to introduce an interface variable ω_Δ defined as the frequency complement that must be added to the available low-frequency signal to recover the high-frequency signal. This complement is defined as

$$\omega_\Delta = \tilde{\omega} - \bar{\omega} \tag{22}$$

and can also be defined using fluctuating quantities by

$$\omega_\Delta = \omega' - \omega'' \tag{23}$$

To evaluate ω_Δ on Ω_c, we propose an enrichment procedure that takes the extrapolated value of ω_Δ defined in Ω_f, where this quantity is easier to obtain. This procedure has to enforce a generalized kinetic energy conservation principle between the field at the current point of Ω_f and the reconstructed field in fine ghost cells in Ω_c. It involves naturally a rescaling of the SGS viscosity defined on coarse cells in order to be adapted to quantities newly defined in the fine ghost cell.

The restriction procedure $\mathbf{R}$ previously described and used in the fine mesh domain Ω_f allows us to obtain a coarse field in each equivalent coarse cell.

In order to compute this low resolution field in each point of the fine mesh domain (as well as in current points and in ghost points), and thus determine the complementary field ω_Δ by subtracting the low resolution field from the high resolution field in Ω_f, one applies a projection operator $\mathbf{P}$. This operator $\mathbf{P}$ is a tri-linear interpolation operator based on Taylor expansions. In three-dimensional form, for discrete treatment, third-order accuracy is obtained by using up to ten coarse cells to define this interpolation operator, yielding the following discrete approximation:

$$\mathbf{P} = Id + O(\bar{\Delta}^3) \tag{24}$$

Numerical experiments have shown the third-order accuracy to be a minimal requirement to obtain reliable results.

At the vicinity of the interface, the ω_Δ field obtained in Ω_f by Equation (22) is then extrapolated to Ω_c by a linear extrapolation operator $\mathbf{E}$ in order to build the enriched field in the ghost cells in Ω_c.

The enrichment procedure, illustrated by Figure 1 can be written as

$$\tilde{\omega}_{\Omega_c} = \mathbf{P}(\bar{\omega}_{\Omega_c}) + \mathbf{E}(\omega_{\Delta\Omega_f}) = \mathbf{P}(\bar{\omega}_{\Omega_c}) + \mathbf{E}(\tilde{\omega}_{\Omega_f} - \mathbf{P}\cdot\mathbf{R}(\tilde{\omega}_{\Omega_f})) \tag{25}$$

Since the enrichment procedure cannot be extended to several rows of ghost cells because of a loss of accuracy and stability in extrapolation procedure **E**, also, the SGS viscosity $\tilde{\mu}_{t\Omega_c}$ cannot be defined in a useful manner (requiring a five point stencil in the case of the discrete treatment of the MSM model). Thus, a SGS viscosity reconstruction procedure in the ghost cells has to be defined.

To compute $\tilde{\mu}_{t\Omega_c}$ we propose to directly rescale $\bar{\mu}_{t\Omega_c}$. In a way, it amounts to rescaling the fluctuating energy $u_i'u_i'$ to $u_i''u_i''$ in order to enforce a generalized kinetic energy conservation. For this purpose, the following relationships, which take into account the cut-off length scale and the sub-grid kinetic energy, are considered to define the sub-grid viscosities $\bar{\mu}_{t\Omega_c}$ and $\tilde{\mu}_{t\Omega_c}$ at the interface

$$\tilde{\mu}_{t\Omega_c} = C\cdot\tilde{\rho}\cdot\tilde{\Delta}\cdot\left(\frac{1}{2}\cdot u_i''u_i''\right)^{1/2} \tag{26}$$

$$\bar{\mu}_{t\Omega_c} = C\cdot\bar{\rho}\cdot\bar{\Delta}\cdot\left(\frac{1}{2}\cdot u_i'u_i'\right)^{1/2} \tag{27}$$

The evaluation of $\tilde{\mu}_{t\Omega_c}$ in the fine ghost cells requires the knowledge of the fluctuating kinetic energy quantity $(u_i''u_i'')^{1/2}$ in Equation (26). Using relationship (23) applied to velocity components, this quantity can be decomposed as

$$u_i''u_i'' = (u_i' - u_{i\Delta})(u_i' - u_{i\Delta}) = u_i'u_i' + u_{i\Delta}u_{i\Delta} - 2\cdot\|\vec{u}'\|\cdot\|\vec{u}_\Delta\|\cdot\cos(\vec{u}';\ \vec{u}_\Delta)$$

Following definition (27) to estimate u', we obtain

$$u_i''u_i'' = \left(\frac{\bar{\mu}_{t\Omega_c}}{C'\cdot\bar{\rho}\cdot\bar{\Delta}}\right)^2 + u_{i\Delta}u_{i\Delta} - 2\cdot\|\vec{u}'\|\cdot\|\vec{u}_\Delta\|\cdot\cos(\vec{u}';\vec{u}_\Delta)$$

Assuming that $\vec{u}$ and $\vec{u}_\Delta$ vectors are aligned, fluctuating energy $u_i''u_i''$ is evaluated as

$$u_i''u_i'' = \left(\frac{\bar{\mu}_{t\Omega_c}}{C'\cdot\bar{\rho}\cdot\bar{\Delta}}\cdot\frac{\vec{u}_\Delta}{\|\vec{u}_\Delta\|} - \vec{u}_\Delta\right)^2 \tag{28}$$

Thus, the reconstructed viscosity $\tilde{\mu}_{t\Omega_c}$ can be estimate from relationships (26) and (28) by

$$\tilde{\mu}_{t\Omega_c} = C'\cdot(\bar{\rho} + \rho_\Delta)\cdot\tilde{\Delta}\cdot\|\vec{u}_\Delta\|\cdot\left|\frac{\tilde{\mu}_{t\Omega_c}}{C'\cdot\bar{\rho}\cdot\bar{\Delta}\cdot\|\vec{u}_\Delta\|} - 1\right| \tag{29}$$

This formulation depends only on $\bar{\mu}_t$, $\bar{\mathbf{U}}$, $\mathbf{U}_\Delta$ variables

$$\bar{\mu}_{t\Omega_c} = \mu_t(\bar{\mu}_t; \bar{\mathbf{U}}; \mathbf{U}_\Delta) \tag{30}$$

and satisfies well the convergence condition: $\tilde{\mu}_{t\Omega_c} \to \bar{\mu}_{t\Omega_c}$ when $\tilde{\Delta} \to \bar{\Delta}$, i.e. when $\|\vec{\omega}_\Delta\| \to 0$. Thus we now have the knowledge of all the quantities necessary to close the reconstruction problem at the interface. The convergence rate of the algorithm is governed by the accuracy to which relationship (16) is approximated (third-order accuracy in the present case). Indeed, for conform meshes the restriction procedure is equal to the identity, and the objection operator stays third-order accuracy

$$\mathbf{R} \to Id$$
$$\mathbf{P} = Id + O(\bar{\Delta}^3)$$
$$\mathbf{P}\cdot\mathbf{R} \to Id + O(\bar{\Delta}^3)$$

Compared with the accuracy of the scheme (second-order accuracy), the convergence rate in $O(\bar{\Delta}^3)$ is acceptable.

Finally, the multi-domain/multi-resolution algorithm for the specific treatment at the interface can be summarized by

available variables at time $n\Delta t$: $\tilde{\mathbf{U}}^n_{\Omega_f}$, $\bar{\mathbf{U}}^n_{\Omega_c}$, $\tilde{\mu}^n_{t\Omega_f}$, $\bar{\mu}^n_{t\Omega_c}$

computation of the filtered values $\bar{\mathbf{U}}^n_{\Omega_f}$ and $\tilde{\mathbf{U}}^n_{\Omega_c}$ using Equations (20) and (25)

computation of the SGS viscosities $\bar{\mu}^n_{t\Omega_c}$ and $\tilde{\mu}^n_{t\Omega_c}$ using Equations (21) and (29)

computation of $\tilde{\mathbf{U}}^{n+1}_{\Omega_f}$, $\bar{\mathbf{U}}^{n+1}_{\Omega_c}$, $\tilde{\mu}^{n+1}_{t\Omega_f}$, $\bar{\mu}^{n+1}_{t\Omega_c}$

5. NUMERICAL METHOD

5.1. Spatial discretization and time integration

Since only subsonic flows without shock are considered in this study, a second-order accurate central discretization is used. In order to reduce the effects of aliasing and truncation errors, the skew-symmetric form is used here for the evaluation of numerical fluxes at the cell faces (see Kravchenko and Moin [21] for theoretical approaches and application with finite difference and spectral methods). In finite volume, this formulation is easily obtained by (see Weber *et al.* [22])

$$\mathbf{F}_{i+1/2} = \mathbf{F}(\mathbf{U}_{i+1/2}) = \mathbf{F}\left(\frac{1}{2}(\mathbf{U}_i + \mathbf{U}_{i+1})\right)$$

The different spatial derivatives (temperature gradients, velocity gradients) present in flux $\mathbf{F}$ are computed via the Green formulae in a same manner as the sum of the flux $\mathbf{F}$. The use of

staggered cells to evaluate gradients ensures the coupling between odd and even cells and prevents spurious wiggles.

The time integration is performed using a third-order three-stage compact Runge–Kutta time stepping scheme [23].

5.2. Forcing term

The governing equations have been modified to be adapted to the physical problem for the plane channel application.

Because of the flow periodicity in the streamwise direction, the flow must be driven by a uniform body force $\mathbf{f}_1$ to preserve a constant mass flow rate across the channel. This force $\mathbf{f}_1$ is equivalent to a mean pressure gradient. The self-adaptive algorithm proposed by Deschamps [24] and used successfully by Lenormand [7,8] for subsonic and supersonic channel flows is employed to compute the driving term at each time step.

6. APPLICATIONS AND RESULTS

The multi-domain/multi-resolution technique developed here has been assessed on a subsonic plane channel flow. This configuration is interesting because of its very simple geometry, and, from a physical point of view, because most of the wall-turbulence interactions are represented in it. Moreover, lots of previous results obtained with LES and DNS computations for this configuration exist and can be used as support for validation. Among these, we refer principally to Lenormand's work [8] who used, in one of his computational cases the same SGS model as in the present study.

6.1. Physical problem and computational parameters

The selected configuration is the isothermal wall plane channel flow. The computational configuration is displayed in Figure 2.

Periodic boundary conditions are used in the streamwise (x) and spanwise (y) directions. For notational convenience, all hat, bar and tilde symbols associated previously with the resolved variables in the equations are left out, and the $\langle \cdot \rangle$ operator is defined as statistical average over time and homogeneous directions ((x, y) planes).

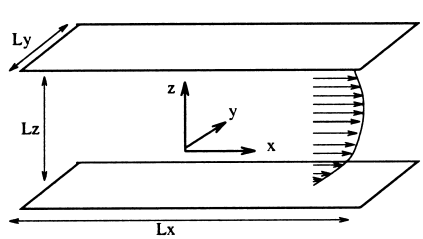

Figure 2. Plane channel configuration.

Two targeted skin-friction Reynolds numbers have been considered: $Re_\tau = 180$ and $Re_\tau = 590$, where Re_τ is defined as $Re_\tau = \sqrt{\rho_w Re(\partial \langle u \rangle / \partial z)_w}$. This corresponds to a Reynolds number based on bulk density ρ_b, bulk velocity u_b, channel half width δ and wall viscosity $\mu_w = \mu(T_w)$ equal to about 3000 and 11000 respectively. The Mach number M_0, defined from the bulk velocity u_b and the mean sound velocity at the wall as $M_0 = u_b/a_w$, is set equal to 0.5. The size of the computational domain was chosen such that the two-point correlations in the streamwise and spanwise directions would be essentially zero at the maximum separation (half the domain size).

In the present work, all the computations have been performed with the Courant–Friedrich–Lewy (CFL) number equal to 0.95. This small value makes it possible that assume that the time-filtering effects due to the use of finite time steps will be masked by the implicit space-filtering operation.

All the mean values presented below are obtained after having averaged on a sample time corresponding to more than ten flow through times, ensuring of full convergence of the first- and second-order statistical moments.

Several computational grids, including both mono- and three-domain cases, have been used to analyse the influence of the mesh ratio across the interface (from 2 to 4) and the location of the interface (with respect to the wall). A mesh ratio at the interface equal to 4 was chosen to be a maximum because a sudden restriction with larger aspect ratio in a turbulent zone is of little significance from a practical point of view (several consecutive sub-domains should preferably be defined). A partial view of the grid for that value of the mesh ratio across the interface is shown in Figure 3. Uniform mesh spacing is used in the homogeneous directions, while a stretched grid following a hyperbolic tangent law distribution is used in the wall-normal direction. All computational parameters are given in Table I. For multi-domain

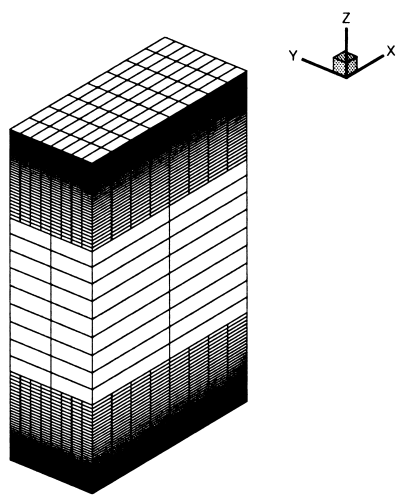

Figure 3. View of a piece of mesh in multi-domain case (de-refinement 4).

Table I. Computational parameters.

Case	Re_τ	L_x^*	L_y^*	$N_x \times N_y \times N_z$	Δ_x^+	Δ_y^+	$\Delta_{z_{\text{wall}}}^+$	z_Γ^+
L_{fine}	180	2π	$4/3\pi$	$41 \times 61 \times 119$	28	12	1	
L_{coarse}	180	2π	$4/3\pi$	$21 \times 35 \times 119$	57	20	1	
A1	180	2π	$4/3\pi$	$41 \times 61 \times 119$	28	12	1	
A-R2	180	2π	$4/3\pi$	$41 \times 61 \times 43$	28	12	1	95
				$21 \times 31 \times 18$	56	24	–	
A-R3	180	2π	$4/3\pi$	$40 \times 61 \times 42$	28	12	1	95
				$14 \times 21 \times 13$	81	36	–	
A-R32	180	2π	$4/3\pi$	$40 \times 61 \times 27$	28	12	1	47
				$14 \times 21 \times 23$	81	36	–	
A-R33	180	2π	$4/3\pi$	$40 \times 61 \times 18$	28	12	1	25
				$14 \times 21 \times 29$	81	36	–	
A-R4	180	2π	$4/3\pi$	$41 \times 61 \times 42$	28	12	1	95
				$11 \times 16 \times 10$	112	48	–	
B1	590	2π	π	$55 \times 121 \times 129$	68	15	1	
B-R2	590	2π	π	$55 \times 121 \times 32$	68	15	1	95
				$28 \times 61 \times 34$	137	24	–	
B-R3	590	2π	π	$55 \times 121 \times 32$	68	15	1	95
				$19 \times 41 \times 23$	206	46	–	

computations, the first (fine) mesh corresponds to the near-wall sub-domain, while the second (coarse) one is related to the core of the channel. The z_Γ^+ is the distance of the interface to the wall expressed in wall units. The size of the mesh expressed in wall units is also shown.

6.2. Mono-domain validation

The first stage of the study consists in validating the code for a classical mono-domain use. A LES was carried out (case A1) at $Re_\tau = 180$, and results are compared with those of Lenormand *et al*. [7,8]. From the results presented in Table II related to the skin friction τ_w, the computed friction Reynolds number Re_τ and the mean centreline velocity, one can observe that the mean values are in good agreement with previous results of Lenormand and more particularly in the case of the coarse mesh. The reason for a better correlation with results in

Table II. Comparison between present mono-domain results and margin of Lenormand's results obtained with different modelling and two different meshes (on a fine mesh (L_{fine}) and on a coarse mesh (L_{coarse})).

Case	τ_w	Re_τ	$u_\tau \times 10^2$	U_c
L_{fine}	10.73 – **11.78** – 13.06	180 – **192** – 202	5.85 – **6.13** – 6.45	1.15 – **1.16** – 1.17
L_{coarse}	10.20 – **10.87** – 13.18	179 – **185** – 203	5.71 – **5.89** – 6.49	1.14 – **1.15** – 1.16
A1	10.65	182	5.84	1.155

Bold values are obtained using the same sub-grid model.

the coarse mesh configuration of Lenormand *et al.* is probably due to the fact that Lenormand's computations were carried out using a fourth-order accurate discretization of the convective fluxes, while the present ones rely on a second-order accurate discretization. Figures 4–6 present comparisons between results obtained in this study and Lenormand's results for the same number of grid points, Mach number and SGS model. The mean velocity profiles normalized with the skin friction in Figure 4 are in very good agreement. Figures 5 and 6 show the root-mean-square (r.m.s.) velocity fluctuations obtained in the present computation. The r.m.s. quantities reach the targeted level close to the walls where the mesh is refined. In the centre part of the channel, some differences exist. These differences could be explained by the difference of accuracy of the schemes, which has an important impact on the quality of results in the central region of channel, where the mesh is very coarse.

6.3. A priori assessment of the SGS viscosity reconstruction procedure

In order to assess the SGS viscosity reconstruction procedure, an *a priori* test has been performed test has been performed using an instantaneous field obtained in the previous mono-domain simulation.

The sub-grid model was first applied to the field, resulting in a corresponding sub-grid viscosity field. The instantaneous field was then restricted using the previously described discrete operator **R** on a coarser grid. The sub-grid model was then applied to this lower-resolution field resulting in a second sub-grid viscosity field. In a third step, the interface reconstruction procedure was applied to the low-resolution field and the associated sub-grid viscosity in order to reconstruct an approximate of the high-resolution field sub-grid viscosity.

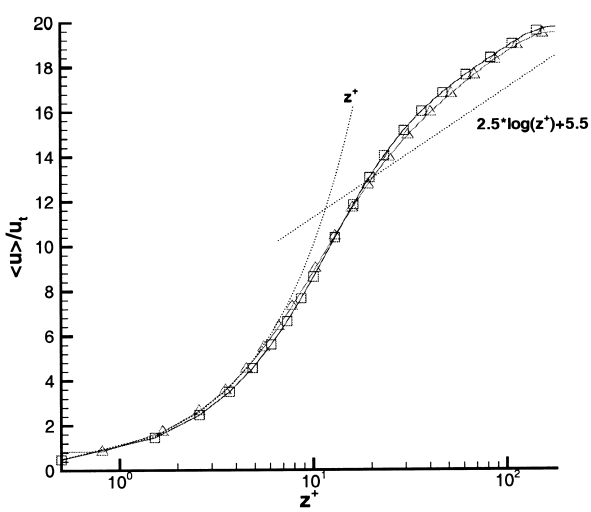

Figure 4. Curve fit of mean velocity profiles in viscous sub-layer and logarithmic region, -□-; Lenormand *et al.*, -△-; law of the wall, —.

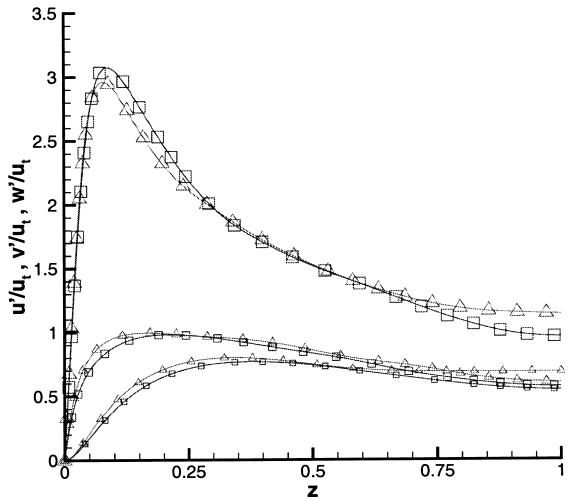

Figure 5. Streamwise, spanwise and wall-normal r.m.s. velocity fluctuations normalized with the skin friction velocity, -□-; Lenormand *et al.*, -△-.

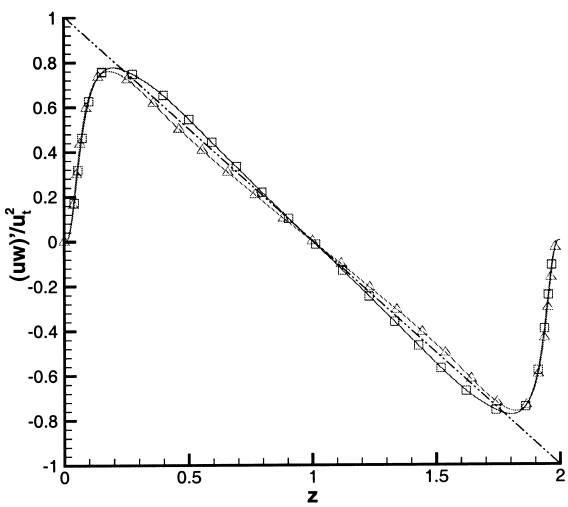

Figure 6. Shear stress normalized with the square of the skin friction velocity, -□-; Lenormand *et al.*, -△-.

Figure 7 presents mean profiles of the three SGS viscosities obtained by averaging over homogeneous directions. One observes that the reconstructed viscosity compares very well with the targeted one—i.e. original SGS viscosity computed on the high-resolution field.

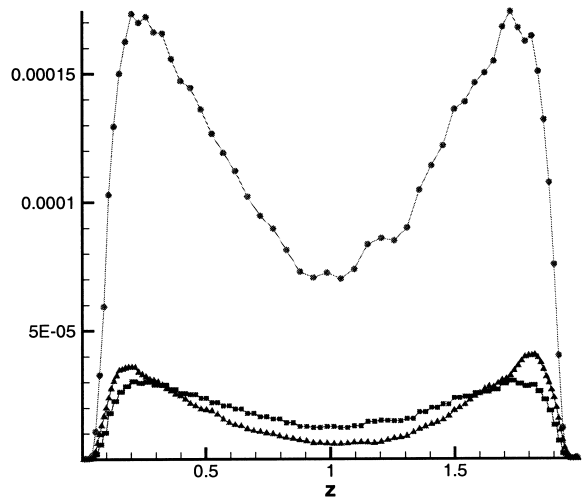

Figure 7. Mean eddy viscosity profiles: eddy viscosity calculated on fine mesh -▲-; eddy viscosity calculated on coarse mesh -●-; reconstructed eddy viscosity -■-.

To analyse more accurately the efficiency of the reconstruction procedure, Figure 8 presents a comparison of the distribution of sub-grid viscosity on the plane $z^+ = 95$. It is seen that the proposed reconstruction procedure is able to capture a correct spatial distribution for the sub-grid viscosity. Although the initial distribution of viscosity is not exactly recovered, maxima and minima of reconstructed viscosity are located in the same place and a similar global level is found again. These different results allow us to conclude positively on the efficiency of the reconstruction procedure.

6.4. A posteriori assessment of the method

The final stage of the study consists in carrying out several multi-domain computations of the subsonic channel flow. Three sub-domain configuration have been retained: a fine resolution sub-domain near each solid wall, and a coarser resolution sub-domain in the centre part of the channel. Computational parameters corresponding to the selected cases are given in Table I. They correspond to several combination of the mesh across the interface (2, 3 or 4), the location of the interface (i.e. its distance from the wall) and the Reynolds number making it possible to test the sensitivity of the proposed method. It is recalled here that a mesh ratio of 4 corresponds to a decrease of the volume of the control cell of 64. Larger values of the aspect ratio across the interface could possibly yield serious numerical problems, making the notion of consistency for the numerical method at the interface more fuzzy.

Computed mean velocity, mean temperature and mean density profiles are presented in Figures 9–12. In all cases, the mean field is observed to be nearly insensitive to the presence of the interface and the agreement with the reference mono-domain results is very good. This demonstrates the ability of the proposed method to recover the first-order statistical moments

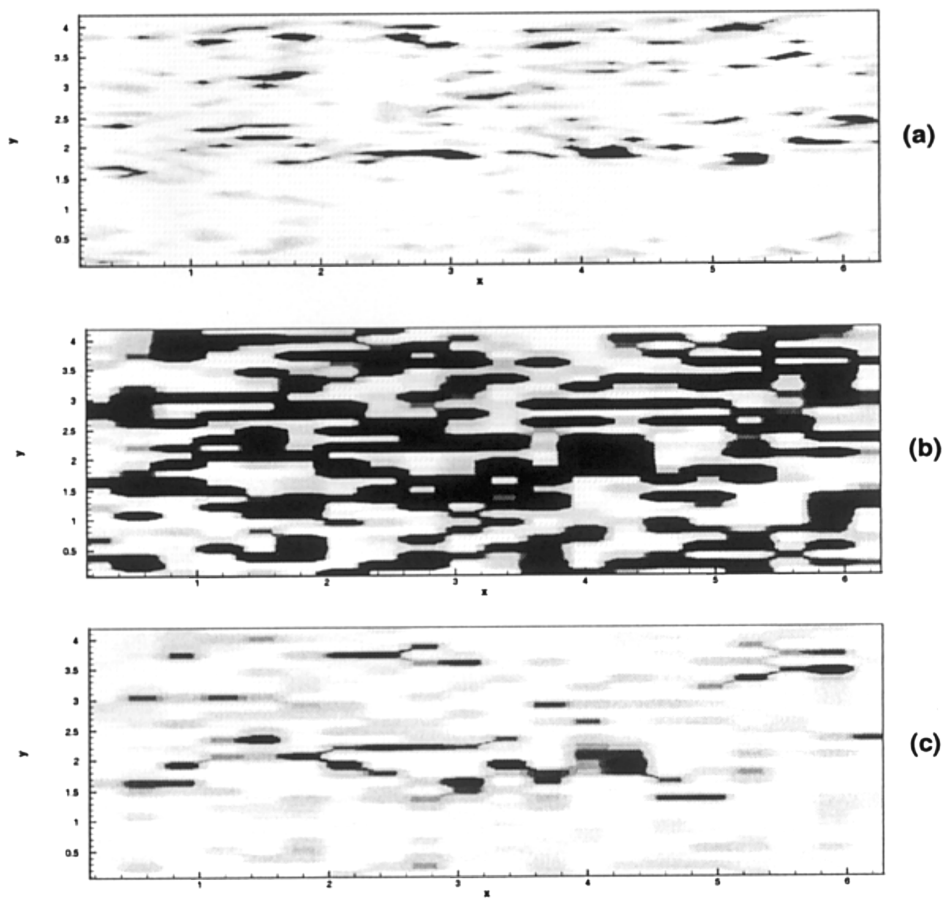

Figure 8. Eddy viscosities at plane $z^+ = 95$. Initial eddy viscosity on primary fine mesh (a); eddy viscosity obtained on coarse mesh after filtering (b); reconstructed eddy viscosity obtained from 'coarse' eddy viscosity on fine mesh (c).

of the flow, even when a mesh ratio of 4 is considered. Main quantities associated to the mean flow field are presented in Table III. It is observed that the skin friction is well predicted and is almost insensitive to the multi-domain decomposition of the grid, except for cases A-R33 and A-R4. This seems to indicate that the interface must be located outside the turbulence production region located in the buffer layer (A-R33 corresponds to an interface very close to that region) in order to not corrupt the prediction of the mean velocity gradient at the wall. The second conclusion is that a mesh ratio of 4 is large enough to yield consequent numerical errors when a second-order accurate method is employed. Both centreline velocity and centreline temperature are very well recovered in all the presented cases.

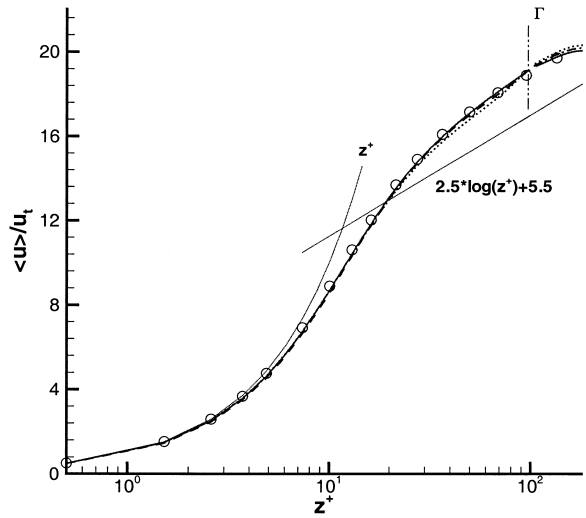

Figure 9. Mean velocity profiles at $Re_\tau = 180$: A1, ●; A-R2, -○-; A-R31, -□-; A-R4, -△-.

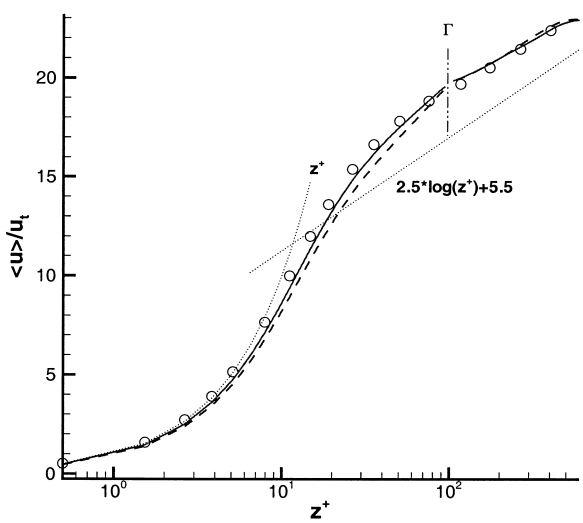

Figure 10. Mean velocity profiles at $Re_\tau = 590$: B1, -□-; B-R2, -△-; B-R3, -○-.

The mean fields presented are continuous. The discontinuity of the instantaneous variables at the interface is related by the sub-grid viscosity displayed on Figure 13 and then expected to be observed on the second-order statistical moments of the solution. As an example,

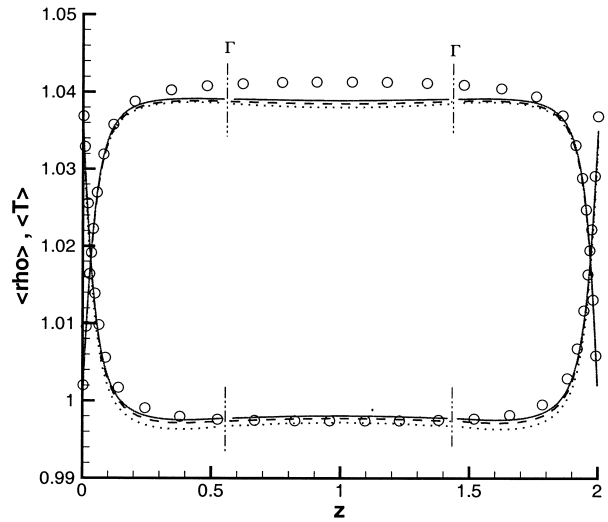

Figure 11. Density (lower curves) and temperature (upper curves) profiles at $Re_\tau = 180$: A1, ●; A-R2, -○-; A-R31, -□-; A-R4, -△-.

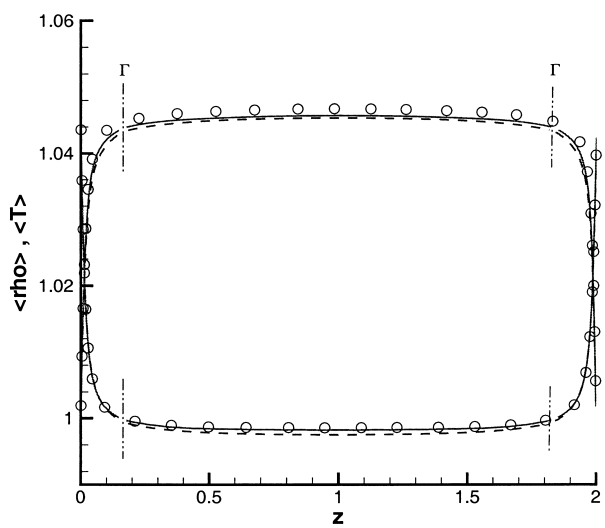

Figure 12. Density (lower curves) and temperature (upper curves) profiles at $Re_\tau = 590$: B1, -□-; B-R2, -△-; B-R3, -○-.

Table III. Comparison global time-averaged data.

	τ_w	Re_τ	$u_\tau \times 10^2$	U_c	T_c
A1	10.65	182	5.84	1.155	1.04
A-R2	10.56	181	5.82	1.16	1.04
A-R31	10.5	180	5.80	1.16	1.04
A-R32	10.5	180	5.82	1.16	1.04
A-R33	10.64	190	6.1	1.155	1.04
A-R4	10.42	179	5.77	1.16	1.04
B1	29.6	582	5.10	1.11	1.045
B-R2	27.5	560	4.95	1.10	1.045
B-R3	27.5	559	4.9	1.08	1.05

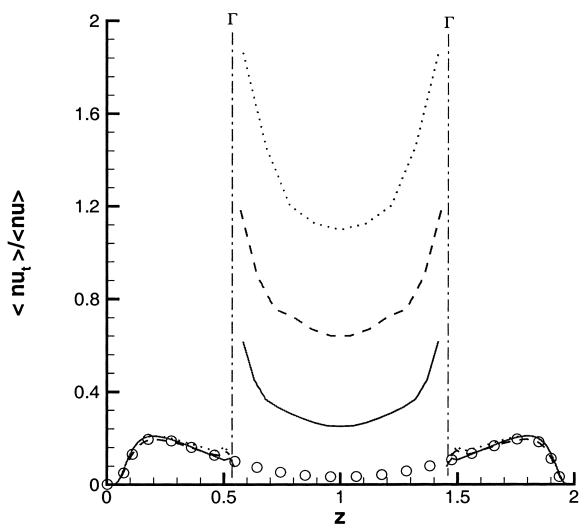

Figure 13. Eddy viscosity profiles at $Re_\tau = 180$: A1, ●; A-R2, -○-; A-R3, -□-; A-R4, -△-.

computed profiles of the rms streamwise velocity components are shown in Figures 14 and 15. Profiles obtained for the other velocity components exhibit the same behaviour and are not shown for want of room. The discontinuity associated to the jump in mesh size across the interface is now clearly seen. As expected, the gap at the interface increases when larger value of the mesh ratio at the interface is used. An interesting feature of the simulation is that the position of the peak (with respect to the solid wall) is not modified by the use of the multi-domain algorithm, neither its amplitude. This fact demonstrates that the near wall dynamics, which is responsible for the skin friction, is captured with the same accuracy as for classical LES. Figure 16 shows that the near-wall dynamics is correctly described, even when the interface is located in the buffer layer ($z^+ = 25$). But it can be observed that the

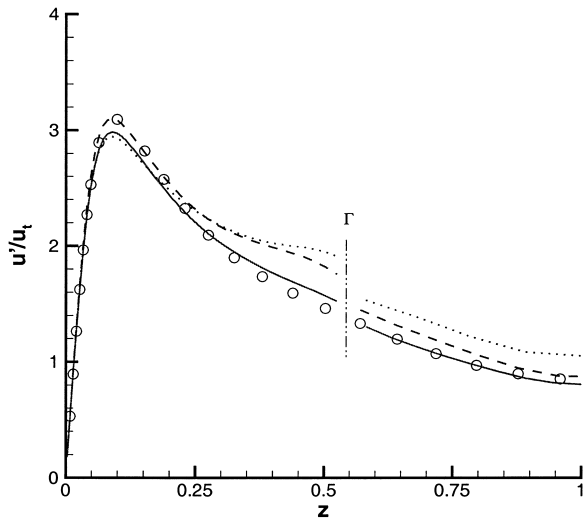

Figure 14. Streamwise r.m.s. velocity fluctuations normalized with the skin friction velocity at $Re_\tau = 180$: A1, ●; A-R2, -○-; A-R3, -□-; A-R4, -△-.

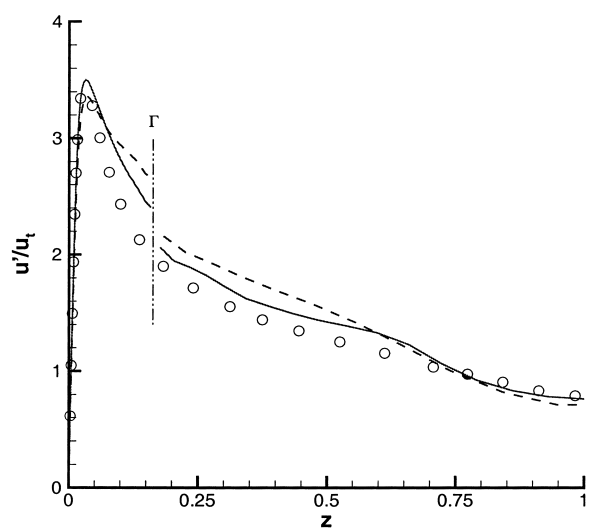

Figure 15. Streamwise r.m.s. velocity fluctuations normalized with the skin friction velocity at $Re_\tau = 590$: B1, -□-; B-R2, -△-; B-R3, -○-.

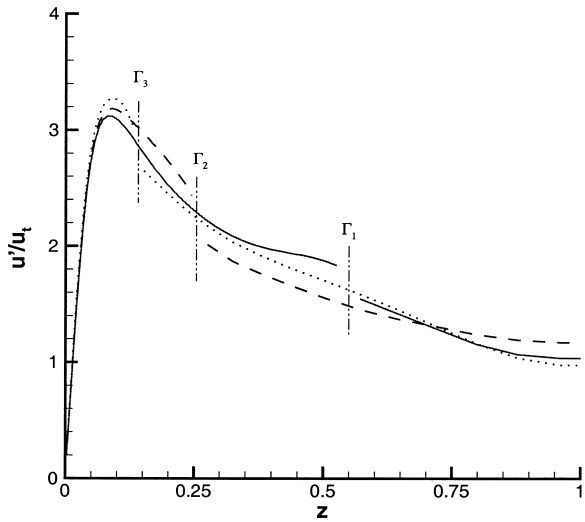

Figure 16. Streamwise r.m.s. velocity fluctuations normalized with the skin friction velocity at $Re_\tau = 180$: A-R31 ($z^+_{\Gamma_1} = 95$), -□-; A-R32 ($z^+_{\Gamma_2} = 47$), -△-; A-R33 ($z^+_{\Gamma_3} = 25$), -○-.

fluctuations are overestimated near the interface on the fine grid side. This may be due to the interpolation error used in the enrichment procedure. Kinetic energy spectra computed in the first plane near the interface on the fine grid side, corresponding to case A1, A-R2 and A-R4 are displayed in Figure 17. It is observed that the expected $k^{-5/3}$ is recovered, but that a bump in the high frequency is present when high mesh aspect ratio across the interface is considered. This is coherent with the idea that the spectral signature of the interpolation cannot be fully controlled. This error is amplified by the fact that the mesh discontinuity occurs in the three space directions.

Nevertheless, the global dynamic of the fluctuations remains physical. The normalized shear stress is presented in Figures 18 and 19. A very good agreement with the mono-domain LES is recovered.

7. CONCLUDING REMARKS

A multi-domain/multi-resolution algorithm for LES of compressible flows, which account explicitly for the cut-off length scale at the domain interface, is proposed and implemented. It is then assessed on the subsonic plane channel configuration. The algorithm is sufficiently accurate to sustain transition and fully developed turbulence.

Several computations have been carried out, corresponding to different combination of the mesh ratio across the interface, the Reynolds number and the position of the interface. Results show that the procedure makes it possible to recover very good results on the mean flow, but

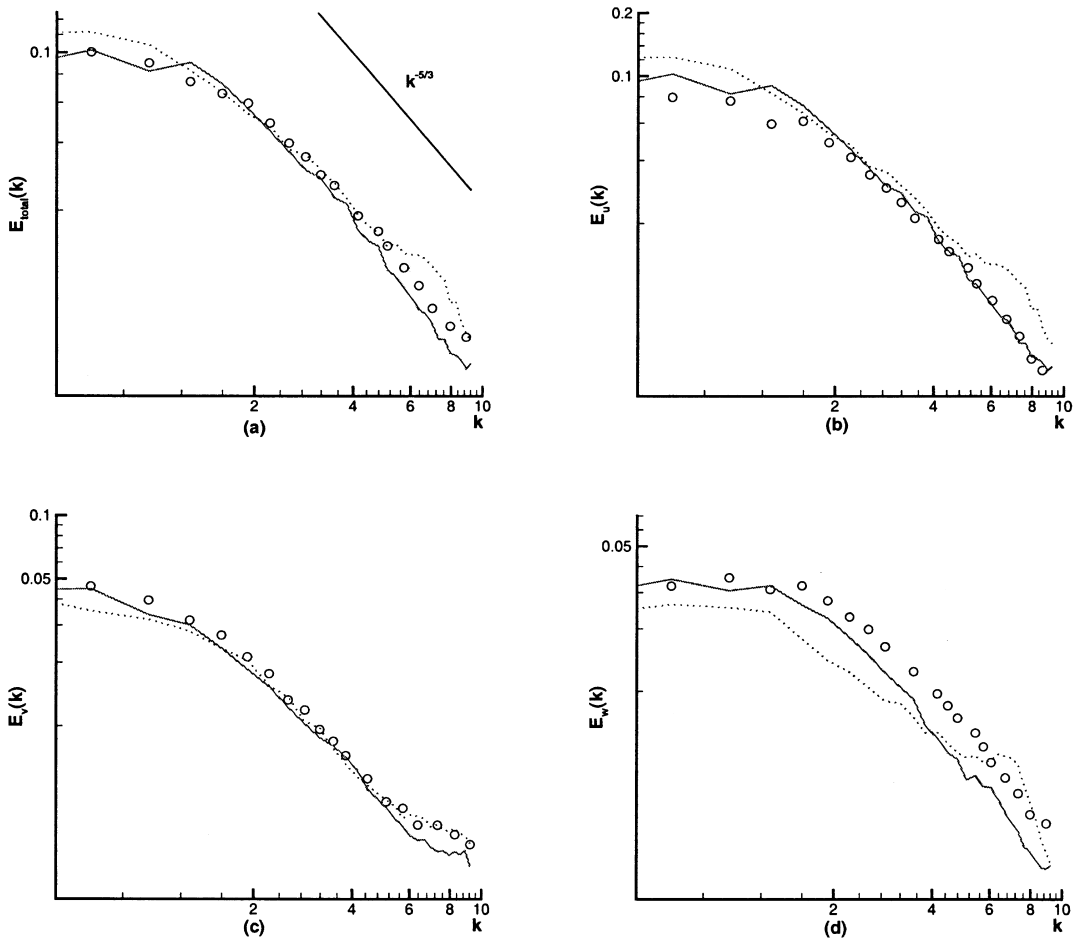

Figure 17. One-dimensionnal energy spectras close to the interface in fine mesh (plane $(z^+ = 95)$: E_{total} (a), E_u (b), E_v (c), E_w (d). A1, -□-; A-R2, -△-; A-R4, -○-.

that second-order moments of the solution are more sensitive to the interface treatment. Nevertheless, the dynamics of the turbulent fluctuations is satisfactorily captured.

One of the most interesting aspects is the significant gain obtained with the multi-domain approach, which makes it possible to use coarser grids in the core of the channel. The memory requirement is reduced and the gain obtained in CPU costs is about 37 and 46 per cent for mesh ratio at the interface equal to 2 and 4 respectively. The simulations performed in this study give some very good results and the method is very attractive in regard to Simons *et al.*'s calculations [1] in terms of CPU costs and quality of the results (five times less CPU time demanded and good agreement between mono-domain and multi-domain results).

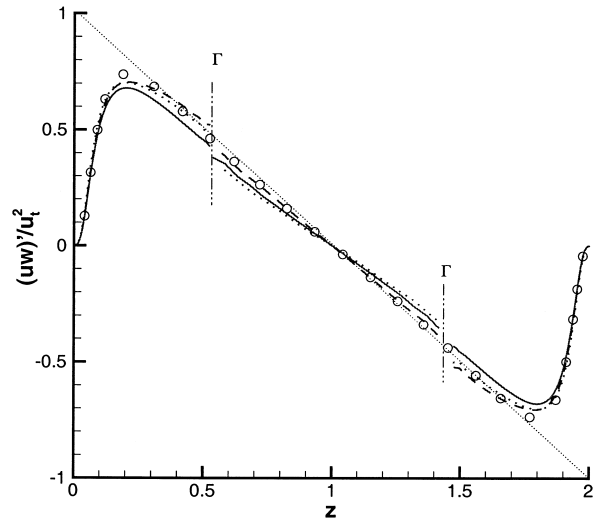

Figure 18. Shear stress normalized with the square of the skin friction velocity at $Re_\tau = 180$: A1, ●; A-R2, -○-; A-R3, -□-; A-R4, -△-.

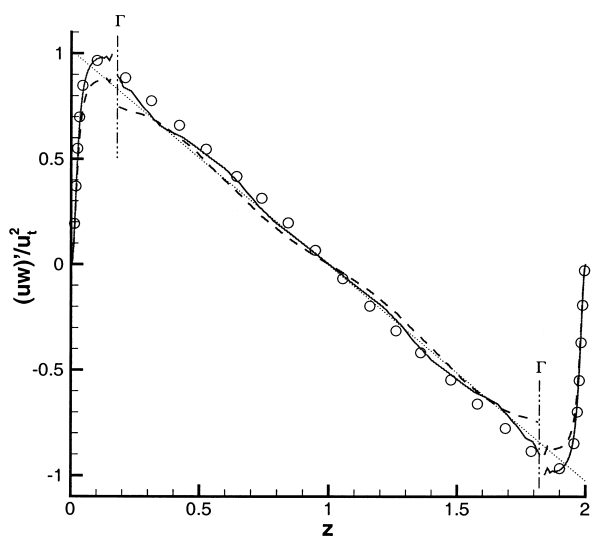

Figure 19. Shear stress normalized with the square of the skin friction velocity at $Re_\tau = 590$: B1, -□-; B-R2, -△-; B-R3, -○-.

REFERENCES

1. Simons TA, Pletcher RH. Large eddy simulation of turbulent flows using unstructured grids. AIAA paper 98-3314, 1998.
2. Rai MM. A conservative treatment of zonal boundaries for Euler equation calculations. *Journal of Computational Physics* 1986; **62**: 472–503.
3. Rai MM. An implicit, conservative treatment of zonal boundaries for Euler equation calculations. *Computers and Fluids* 1986; **14**(3): 295–319.
4. Kallinderis Y. Numerical treatment of grid interfaces for viscous flows. *Journal of Computational Physics* 1992; **98**: 129–144.
5. Kravchenko AG, Moin P, Moser R. Zonal embedded grids for numerical simulations of wall-bounded turbulent flows. *Journal of Computational Physics* 1996; **127**: 412–423.
6. Kravchenko AG, Moin P, Shariff K. B-spline method and zonal grids for simulation of complex turbulent flows. *Journal of Computational Physics* 1999; **151**: 757–789.
7. Lenormand E, Sagaut P, Phuoc Loc T. Large-eddy simulation of compressible channel flow at moderate Reynolds number. *International Journal for Numerical Methods in Fluids* 2000; **32**: 369–406.
8. Lenormand E, Sagaut P, Ta Phuoc Loc L, Comte P. Subgrid-scale models for large-eddy simulation of compressible wall bounded flows. *AIAA Journal* 2000; **38**(8): 1340–1350.
9. Favre A. Equations stastistiques aux fluctuations turbulentes dans les écoulements compressibles: cas des vitesses et des températures. *CR Academie des Sciences de Paris* 1971; **273**: 29.
10. Vreman B, Geurts B, Kuerten H. *A priori* tests of large-eddy simulation of compressible plane mixing layer. *Engineering and Mathematics* 1995; **29**: 299–327.
11. Vreman B. Direct and large-eddy simulation of the compressible turbulent mixing layer. Thèse de l'Université de Twente, 1995.
12. Moin P, Squires K, Cabot W, Lee S. A dynamic subgrid-scale model for compressible turbulence and scalar transport. *Physics and Fluids A* 1991; **3**(11): 2746–2757.
13. Sagaut P. *Large-eddy Simulation for Incompressible Flows*. Springer: Berlin, 2001.
14. David E. Modélisation des écoulements compressibles et hypersoniques: une approche instationnaire. Doctorat, Institut National Polytechnique de Grenoble, 1993.
15. Sagaut P, Grohens R. Discrete filters for large-eddy simulation. *International Journal for Numerical Methods in Fluids* 1999; **31**: 1195–1220.
16. Magnient JC, Sagaut P, Deville M. A study of build-in filter for some eddy-viscosity models in large-eddy simulation. *Physics of Fluids* to appear.
17. Stolz S, Adams NA. An approximate deconvolution model procedure for large-eddy simulation. *Physics of Fluids* 1999; **11**(7): 1699–1701.
18. Geurts B. Inverse modeling for large-eddy simulation. *Physics and Fluids* 1997; **9**(12): 3585–3587.
19. Domaradzki JA, Loh KC. The subgrid-scale estimation model in the physical space representation. *Physics of Fluids* 1999; **11**(8): 2330–2342.
20. Domaradzki JA, Yee PP. The subgrid-scale estimation model for high Reynolds number turbulence. *Physics of Fluids* 2000; **12**(1): 193–196.
21. Kravchenko AG, Moin P. On the effect of numerical errors in large-eddy simulations of turbulent flows. *Journal of Computational Physics* 1997; **131**: 310–322.
22. Weber C, Ducros F, Corjon A. Large-eddy simulation of complex turbulent flows. AIAA Paper 98-2651, 1998.
23. Lowery PS, Reynolds WC. Numerical simulation of a spatially-developing, forced, plane mixing layer. Report of the Stanford University, TF 26, 1986.
24. Deschamps V. Simulation numérique de la turbulence inhomogène incompressible dans un écoulement de canal plan. Note Technique ONERA, France, 1988.

